Accepted Manuscript

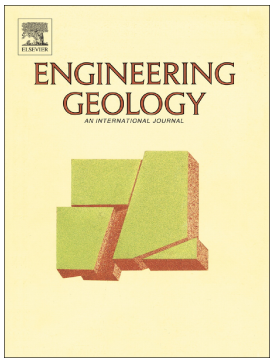

Characteristics and dynamic runout analyses of 1983 Saleshan landslide

Chao Kang, Fanyu Zhang, Fazhen Pan, Jianbing Peng, Weijiang Wu

PII: S0013-7952(17)31822-7
DOI: doi:10.1016/j.enggeo.2018.07.006
Reference: ENGEO 4885

To appear in: *Engineering Geology*

Received date: 14 December 2017
Revised date: 4 July 2018
Accepted date: 4 July 2018

Please cite this article as: Chao Kang, Fanyu Zhang, Fazhen Pan, Jianbing Peng, Weijiang Wu , Characteristics and dynamic runout analyses of 1983 Saleshan landslide. Engeo (2018), doi:10.1016/j.enggeo.2018.07.006

Characteristics and dynamic runout analyses of 1983 Saleshan landslide

Chao Kang [a, b], Fanyu Zhang [a*], Fazhen Pan [a], Jianbing Peng [c*], Weijiang Wu [d]

[a] MOE Key Laboratory of Mechanics on Disaster and Environment in Western China, Department of Geological Engineering, Lanzhou University, Lanzhou 730000, China

[b] Department of Civil and Environmental Engineering, University of Alberta, Edmonton, Alberta, T6G 2W2, Canada

[c] Department of Geological Engineering, Chang'an University, Xi'an 710054, China

[d] Geological Hazards Research and Prevention Institute, Gansu Academy of Sciences, Lanzhou 730000, China

* Corresponding author: Zhangfy@lzu.edu.cn and dicexy_1@chd.edu.cn

Abstract

In 1983, a catastrophic landslide occurred in Saleshan, Dongxiang, Gansu, China, which resulted in the death of 237 people and the destruction of 585 houses. Saleshan landslide was a typical rapid moving landslide in loess area, China, which moved with extremely high speed and long run-out distance on a gentle sliding surface. This paper reviews the characteristics of the landslide and its consequence, analyzes the possible triggers and the processes of development, and back-calculates the kinematic characteristics of the landslide. The digital elevation models (DEMs) of the study area before and after the event were used to analyze the geomorphological characteristics before and after the event. The authors inferred the possible deformation and failure processes of the landslide based on available observations. Direct shear tests were carried out to obtain the parameters of the soil involved in the failure and post-failure process, which was adopted in the following simulation using an energy-based runout model. The velocities of moving materials at a different time stage together with the variation of runout distance and maximum flow height are presented. The authors also compared the calculated results with field observations and previous simulation results. Sensitivity analysis was conducted to understand the effect of internal and basal friction angles on the kinematic characteristics. This study indicates that the Saleshan landslide was a fast-moving landslide with long traveling distance. The landslide lasted more than one minute with a maximum velocity of approximately 25 m/s according to the calculation using the energy runout model, which was consistent with the estimations based on the observation of eyewitness. This study also gives an insight on the progressive failure mechanism and explains the high mobility of Saleshan landslide in details, which provides a reference for hazard zonation for areas along loess platforms.

Keywords: Saleshan landslide, loess, kinematic characteristics, energy-based runout model.

1. Introduction

Landslides are an important process which posed significant hazards, resulting in fatalities, property damage and degrading farmland (Huang, 2009). From 2004 to 2010, 2620 fatal landslides were recorded, which resulted in a total of 32,222 recorded fatalities (Petley, 2012). In China, most of the landslides occurred in high-altitude regions such as Qinghai-Tibet plateau and southwest area in China (Huang, 2007). According to the statistical data provided by the Ministry of Land and Resources of the People's Republic of China, landslide geohazards have caused 4,718 fatalities from 2004 to 2016 (Zhang and Huang, 2018).

Every year, one-third of the geohazards in China occur on the Loess Plateau (Zhou et al., 2002), with more than 80% involving landslides with slip surfaces shallower than 10 m (Zhuang et al., 2017). The main types of landslides involving substantial amounts of loess include flow, fall and slide (Li et al., 2013; Hungr et al., 2014; Zhang et al., 2012). According to the field investigation, it was found that most of the landslides in the loess area occurred on a slope around 20° - 35° and the flowslides had a long runout distance due to soil liquefaction resulting in a low frictional angle (Zhang et al., 2009; Zhang et al., 2013; Zhang et al., 2014). Since 1900, more than 20 catastrophic landslides have been recorded whose volumes are greater than 20×10^6 m^3, several of which occurred in loess area of China (Derbyshire et al., 2000; Wen et al., 2004; Huang, 2007; Wang et al., 2014; Xu et al., 2014; Zhang et al., 2014; Zhang and Wang, 2018) (Table 1). The landslides triggered by Haiyuan Earthquake 1920, are typical examples of these cases which in total resulted in more than 100,000 deaths (Huang, 2007; Wang et al., 2014).

Table 1: Summary of the landslides occurred in Loess area with a volume larger than 20 $\times 10^6$ m^3 since 1900 (revised from Wen et al. 2004 and Huang 2007)

Name	Location	Date	Volume ($\times 10^6$)	Possible trigger	Casualties	Reference
Sunjiagou Landslide	Jingning, Gansu	Dec 16, 1920	20	Earthquake	—	Wen et al. (2004)
Dangjiacha Landslide	Haiyuan, Ningxia	Dec 16, 1920	21	Earthquake	—	Wang et al. (2014)
Wolongsi	Boji, Shanxi	Aug 18, 1955	20	Rainfall	28 casualties	Li et al. (2011)
Xipo	Liangdang, Gansu	Feb 15, 1956	65.55	Rainfall	—	Wang (1988)
Chahan Temple Landslide	Xunhua, Qinghai	Nov 14, 1961	100	Rainfall	—	Wen et al. (2004)
Beichuan	Xining, Qinghai	Aug 1974	60	—	—	Wen et al. (2004)
Jingou	Lanzhou, Gansu	Nov 07, 1979	20	Rainfall	13 deaths	Chen et al. (2012)
Saleshan Landslide	Dongxiang, Gansu	Mar 07. 1983	31	Creep, freeze and thawing, brittle failure	237 deaths	Zhang et al. (2002); Wu and Wang (2006)

The Saleshan landslide was a catastrophic landslide in loess area which resulted in the death of 237 people and the destruction of 585 houses. Zhang et al. (2002) explored the possible failure mechanism of this landslide. Li et al. (2013) investigated the mechanical properties of soil samples. Miao et al. (2001) and Liu et al. (2000) studied the post-failure process of Saleshan landslide using a runout model based on the Newton's Second Law. Li et al. (2012) applied a grey system model, a plant growth model and linear combination of the models to calculate the displacement of Saleshan landslide. Although many researchers have studied the kinematic characteristics of this event, the reasons behind the rapid movement and long runout distance of this landslide remain unclear. In the simulation by Miao et al.

(2001), the significant fluctuation was observed in the calculated velocities because of the great uncertainties involved in the calculation of the inter-slice force.

This paper carries out a comprehensive review of Saleshan landslide through reviewing the previous work on Saleshan landslide and analyzing the possible deformation and failure processes according to field observations and laboratory results. More detailed information is included in the paper to support hypotheses of the failure mechanism. An energy-based runout model is adopted to understand the kinematic characteristics of Saleshan landslides, in which the internal energy dissipation due to the deformation of slides in the moving process is considered. The results are validated and compared with previous estimations and discussed based on the comparison with previous publications. The effect of internal and basal frictional angles on the simulation results is also studied.

2. Characteristics of Saleshan landslide

Saleshan landslide is located in Dongxiang County, Gansu Province, China. It occurred at 17: 46 on March 7, 1983 (Figure 1a). Figure 1b and Figure 1c show the 3D view of the landslide and photography taken one month after the sliding, respectively.

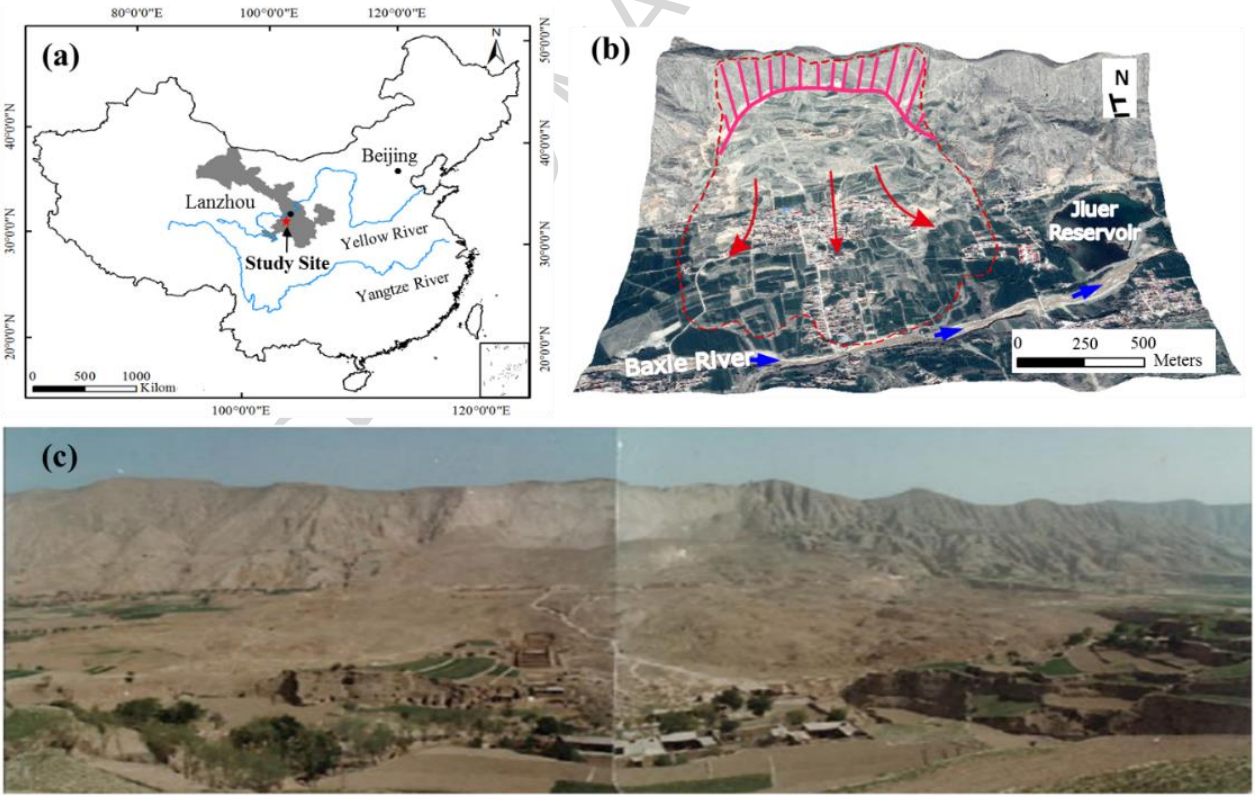

Figure 1: Geographical location of the Saleshan landslide. (a) Location of the Saleshan landslide in Gansu, China; (b) three-dimensional (3D) view of Saleshan landslide (Modified Google Earth Image); (c) Panoramic photography of Saleshan landslide taken 1 month after the sliding (Zhang et al., 2002)

2.1. Geological and geomorphological conditions

The Saleshan landslide is located in the Linxia-Lintao Basin, formed in Late Cenozoic deformation. Two folded belts are situated at the North and South of Saleshan, which are named as Maxianshan-Xinglongshan and Taizishan. The Baxie River, a third-order tributary of the Yellow River, is approximately 800 m away from the toe of the Saleshan, and flows eastward. On the west side of Saleshan, four landslides have been reported (Figure 2), which from close to far, are Bafengshan landslide, Wujia landslide, Zhaojiashan landslide and Nalesishan landslide. Two potential landslides are located on the east side of Saleshan, which are Wangjiashan landslide and Shilaquanshan landslide (Su, 1986).

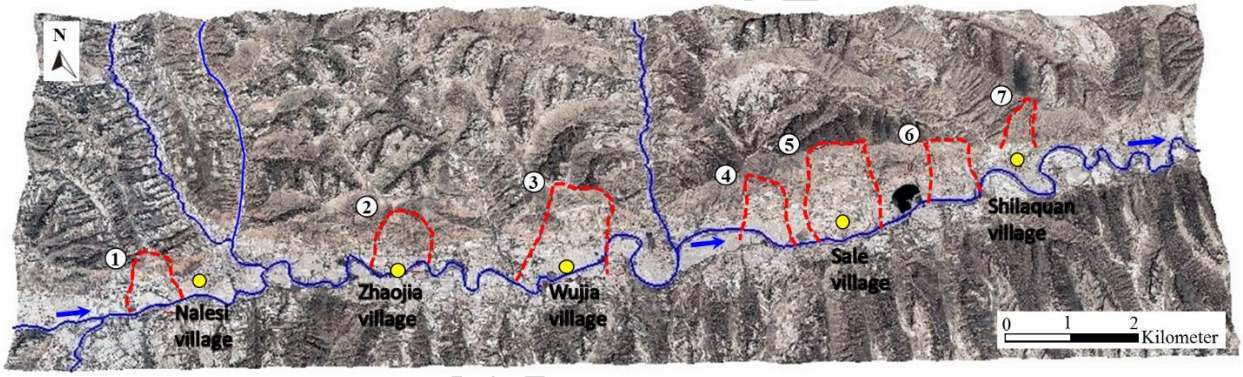

Figure 2: Distribution of occurred and potential landslides in the north bank of Baxie river. 1) Nalesishan landslide (>200 years ago); 2) Zhaojiashan landslide (>100 years ago); 3) Wujia landslide (approximately 50 years ago); 4) Bafengshan landslide (1968); 5) Saleshan landslide (1983); 6) potential landslide in Wangjiashan; 7) potential landslide in Shilaquanshan. (adapted from Su (1986))

The Saleshan slope is formed of the Middle Pleistocene Malan Loess (Q^2_3), overlying Late Pleistocene Lishi Loess (Q_2), and the sub-horizontal (<5°) Pliocene mudstone in sequence. Q^2_3 is pale yellow loose porous loess (e = 0.89) with a thickness ranging from 45 m to 55 m (Zhang et al., 2002). Q_2 is pale brownish-yellow dense loess (e = 0.66) with calcareous concretions in the soil, which is 50 m - 70 m in thickness. Vertical joints are easily detected in both Q^2_3 and Q_2. The alluvial sand and gravel, 10 m – 15 m, are distributed from the toe of the slope to the river valley (Zhang et al., 2002).

Figure 3 shows the longitudinal profile before the landslide, which is revised from Zhang and Wang (1984). The base of the landslide was composed of Pliocene mudstone above which 10-15m thick alluvial sand and gravel were detected at the toe of the slope. The average slope angle at the north the mountain was 13° - 17°. The north side of the mountain was steep. The slope angle above the elevation of 2100 m was 30° – 35° (Zhang et al., 2002).

The flow rate of Baxie river varies seasonally, from 0.2 m^3/s, in the dry season, to 40 m^3/s, in flood period. Yu and Yang (1988) concluded that human activities contributed to the development of Saleshan landslide, including irrigation of farmland at the platform behind the slope and construction of No.92 Reservoir after 1970, which was located approximately 400 m from the toe of the Saleshan. It was also recorded the snowfall in the winter of the previous year was more than the average value (Yu and Yang, 1986).

Figure 3 indicates the river terraces along the Baxie river. The first level terrace is 600 m - 800 m in width. After the event, the deposition zone covered the alluvium at the toe of the slope (Figure 1b) and blocked Baxie River. The second terrace is approximately 20 m above the river level. The bottom third and fourth terraces are covered by Pleistocene Malan Loess. When the landslide occurred, a person living nearby was working on the slope (Huang, 2007). He tightly held the tree in Figure 3 and moved together with the tree for about 960 m, and finally survived without any injuries after the landsliding.

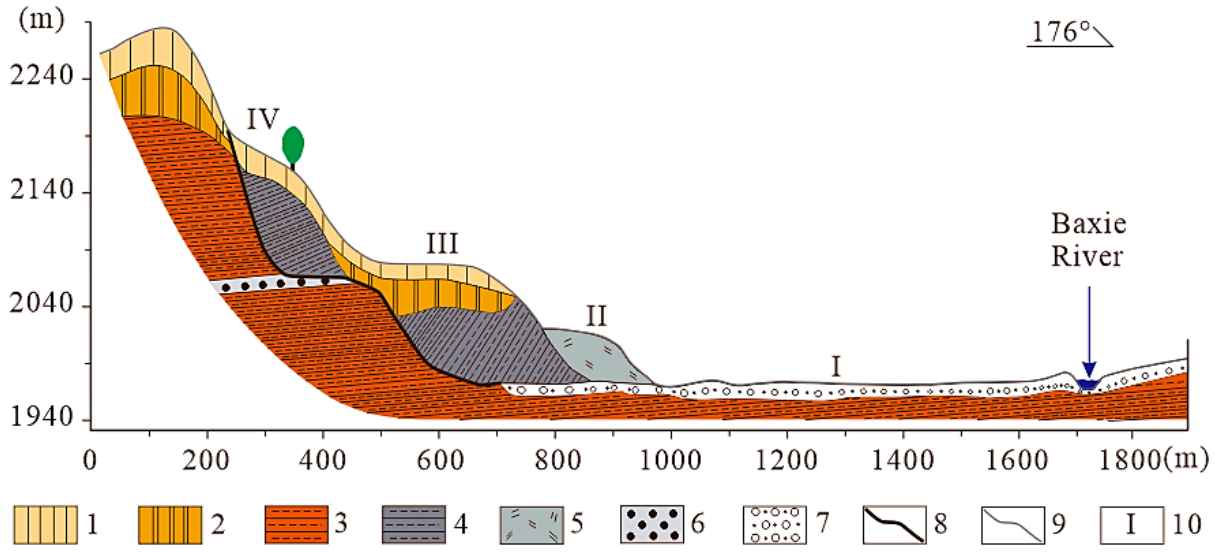

Figure 3: Geologic geomorphologic section of Saleshan landslide before sliding. 1) Malan Loess; 2) Lishi Loess; 3) Pliocene mudstone; 4) Ancient landslide body; 5) Alluvial loess; 6) Cobblestone; 7) Alluvial sand and gravel; 8) Surface of rupture of the old landslide; 9) Ground line; 10) River terraces.(adapted from Zhang and Wang (1984) and Zhang et al. (2002))

The elevation of the studying area ranges from 1950 m to 2280 m (Figure 4a). The length of the slide is 1600 m, and the width ranges from 600 to 1100 m (Zha, 1983 and Zhang et al., .2002). The elevation difference between the toe and the crest of the slope is 220 m. According to the borehole information (Wu and Wang, 2006), the thickness of the landslide on the north side varies from 30-75m. In comparison, the landslide thickness on the south side close to Baxie River is 5-25 m. The area covered by the landslides is

close to 1.3 km^2. The maximum surface relief is more than 20 m in the slope (Figure 4b), and the maximum slope angle is larger than 50º (Figure 4c). Figure 4d indicates the runoff concentration path of the study area. The overflow in the study area is accumulated in the reservoir on the southeast of the final deposition fan.

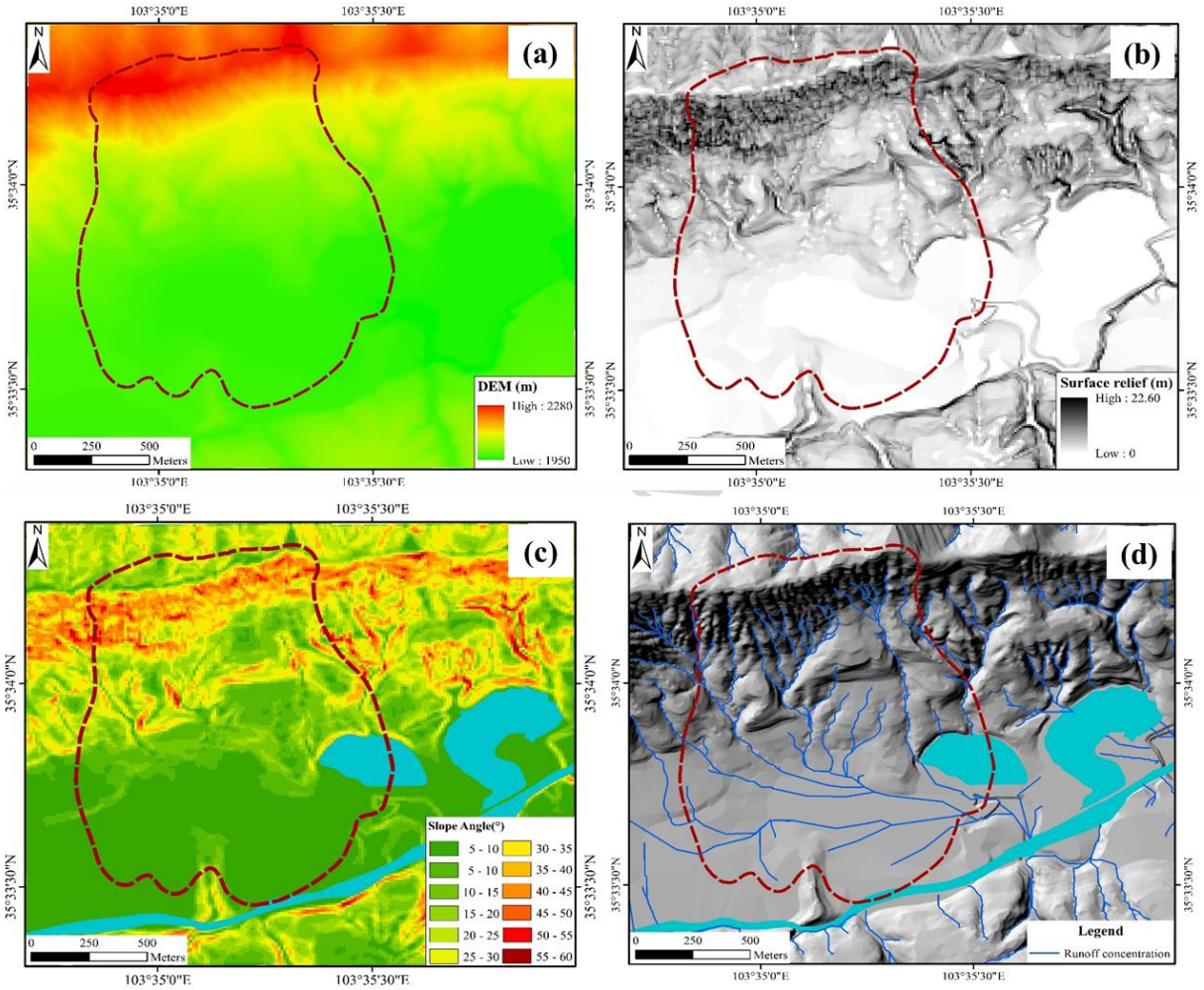

Figure 4: Geomorphological characteristics of Saleshan landslide before the occurrence. (a) Elevation; (b) surface relief; (c) Slope angle; (d) Runoff concentration path.

2.2. Development process and kinematic characteristics

In 1979, a 10 cm wide and 10 m long crack was observed behind the crest of the slope (Zha, 1983) and developed along a pre-existing bedding plane (Zhang et al., 2002). According to the increased width of the cracks, Zhang et al. (2002) classified the development process into four stages: steady fracturing, accelerating fracturing, fracture closing due to rotational displacement, and sliding (Figure 5). The recorded maximum crack width in steady fracturing stage was less than 60 cm which then increased to

more than 150 cm in the accelerating fracturing stage. The crack was closed before the slope started moving (Huang et al., 2016).

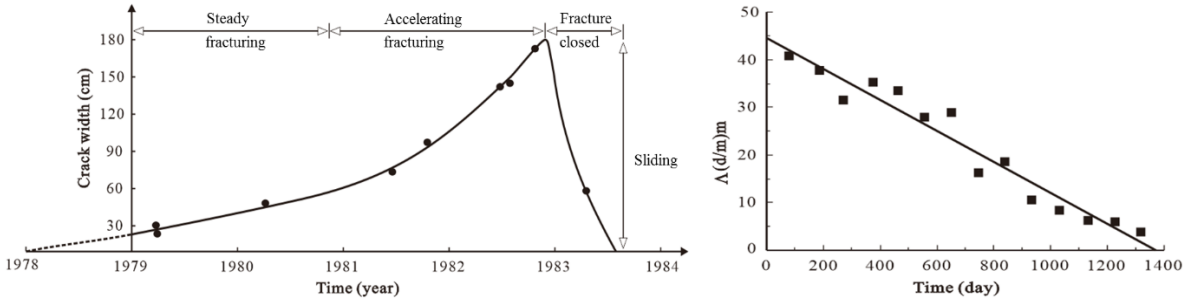

Figure 5: Slope deformation before the sliding of Sale Mountain landslide. (a) The width-time relationship for development of tensile fissure on top of Sale Mountain (Zhang and Wang, 1984), (b) Λ-t space of the tensile fissure (Λ is 1/v (v is velocity), and t is time).

Based on the analysis of local geological and geomorphological characteristics, and the comparison of similar landslides occurred in South Jingyang Platform (Peng et al., 2018), we inferred the possible failure process as illustrated in Figure 6. Figures 6a, 6b, and 6c indicate the pre-failure process of the slope. Figure 6a shows the initial stage of the slope without cracks in the slope. Since a layer of cobblestone was located between two layers of Pliocene mudstones and the variation of the height of sliding surface was more than 100 meters, the shear surface was very difficult to be formed. Therefore, it was very likely that internal weathering and loss of structural strength over a very long period resulted in the progressive failure of the soil in the slope, which was evidenced by the cracks few meters behind the crest of the slope (Zha, 1983) (Figure 6b). In this stage, cracks were only formed at the top mountain, and a possible plastic zone horizontally exited at the toe of the slope (Zhang et al., 2002). After a period with water supply from precipitation and irrigation by locals living on the platform which may be few years, the infiltration of the water resulted in the formation of drainage path and the rising of the water table. A local shear zone underneath the potential sliding body was then formed, resulting from the progressive failure of the soil due to weather soil and development of fissures and cracks in the soil. This stage may last a few decades. As indicated by Petley et al. (2005), the local shear surface could be formed in the slope and extended to the toe and crest of the slope.

After a long period of deformation and creeping, the remaining shear resistance in the soil was mainly provided by the brittle bonds in the overlying loess. The whole slope failed when the shear stress overcame the shear resistance in the shear zone, which was dominated by a brittle failure of the cementation bonds (Huang et al., 2016). This was indirectly evidenced by the thunderous sound heard by residents and the directional alignment of muscovite in the samples from rupture surface under scanning

electron microscope. Upon formation of the slip surface, a sudden acceleration of the landslide movement occurred. This caused undrained loading of the materials at the toe of the slope (Figure 6c). At this stage, pore water pressure existed at the toe of the slope due to the sudden movement of the soil. The trees on the slope inclined as a consequence of slope deformation (Figure 6c). Zhang et al. (2002) also inferred that the development of failure surface was a step-by-step progressive process rather than an entire instantaneous failure. Li et al. (2013) studied the mechanical properties of soil samples from Saleshan landslide using triaxial tests under consolidated undrained conditions under a range of moisture contents, indicating that effective cohesion drops dramatically with the increase of water content. However, the variation of water content has a negligible effect on the effective friction angle, which ranges from 20º to 25º

Figures 6d, 6e and 6f show the post-failure process of the slope. Boreholes information from the Geological Survey of Gansu Province (Figure 7) indicates that the toe of the slope moved. After the soil detached from the original location, the loess instantaneously transferred into a frictional mass from the cemented material. The failed material traveled on the alluvial sand with high mobility, which limited the dissipation of the pore water pressure and resulted in the liquefaction of the alluvial sand with high water content which can be evidenced by the liquefied soil observed at the front of the landslide (Wu and Wang, 2006). Stages d to f were finished in few minutes as witnessed by the residents (Zhang et al., 2002). The landslide body continued moving until the dynamic energy was dissipated due to the frictional forces. The failure material traveled with a long distance and reached the north bank of the Baxie river according to the final investigation (Wang et al., 1988; Zhang et al., 2002; Wu and Wang, 2006). Figure 6e indicated the status of the slope right after stopping. The trees on the sliding body moved with a long travel distance, one of which had saved a person working on a farm (Figure 6d). Since the dissipation of the water content cannot be finished right after the movement, the pore water pressure can possibly be detected underneath the deposited material (Figure 6e). After a period, the water in the soil at the toe of the slope kept dissipating until adapted to the surrounding stress environment (Figure 6f).

e

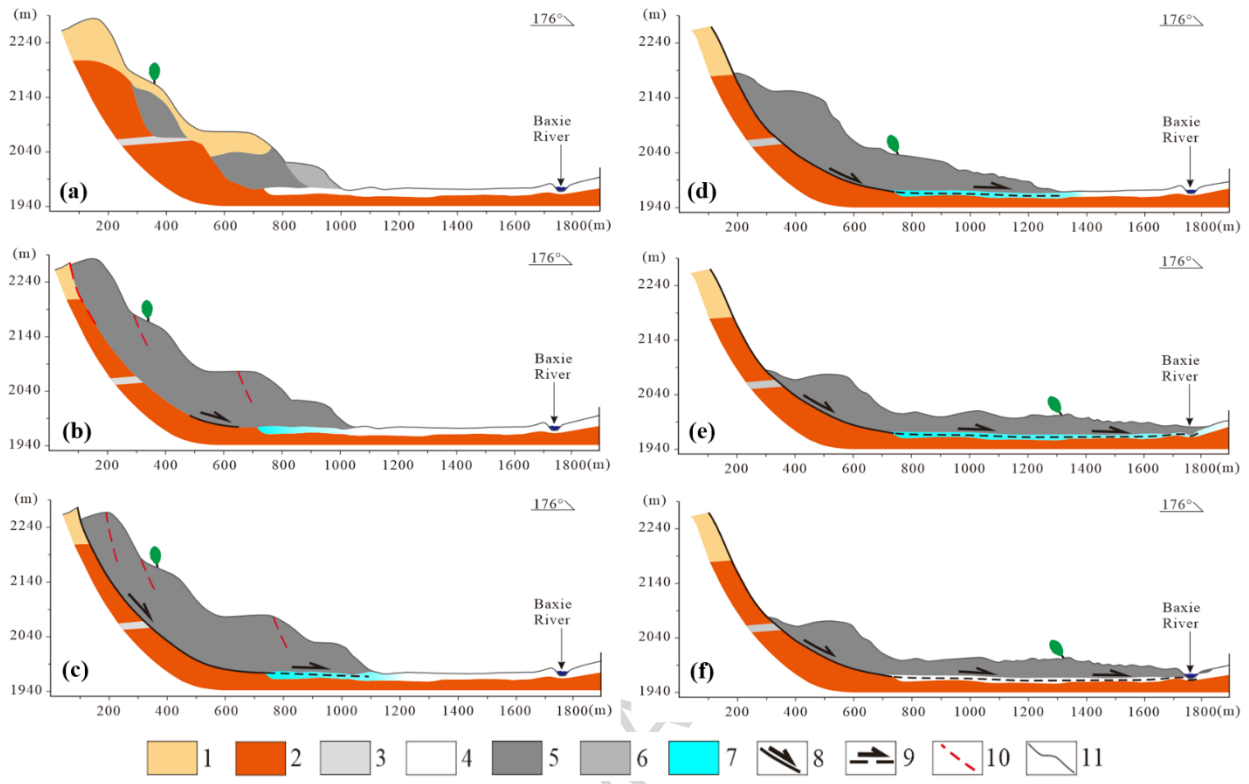

Figure 6: A hypothesized sequence of events leading to the catastrophic failure of 1983 Saleshan landslide. 1) Loess; 2) Pliocene mudstone; 3) Cobblestone; 4) Alluvial sand and gravel; 5) Landslide body; 6) Alluvial loess; 7) Zone with high pore-water pressure; 8) Sliding surface; 9) Inferred sliding surface; 10) Fissure; and 11) Ground surface line.

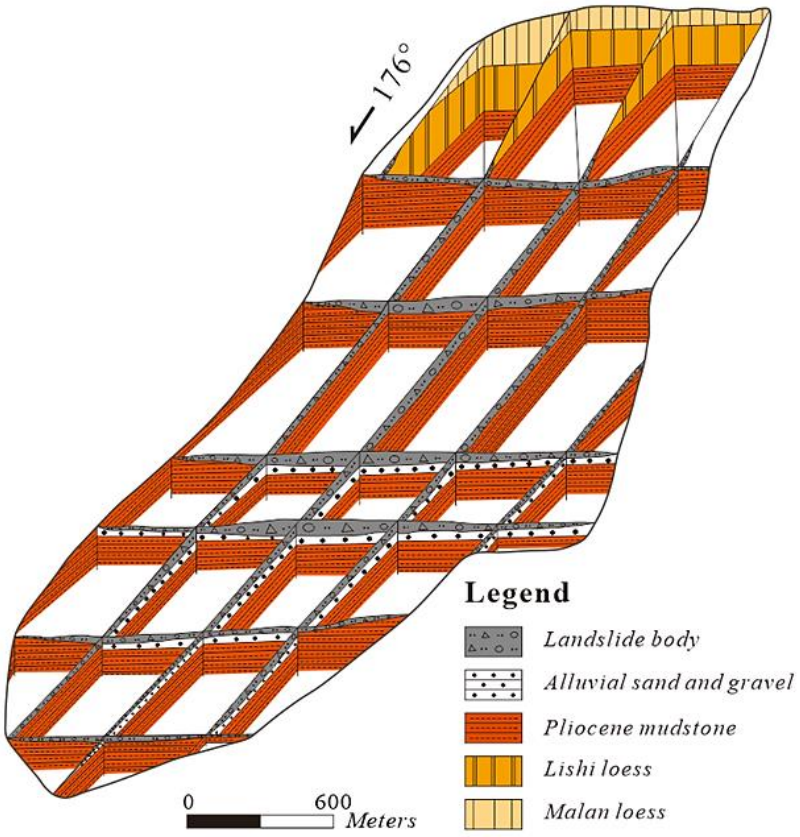

Figure 7: Fence diagram of Saleshan landslide after failure (adapted from Su (1986))

According to final calculation, the total volume of soil detached from the source area was approximately 3.1×10^7 m^3, and the displaced materials traveled 1050 m horizontally and dropped down 203 m in the vertical direction. According to Li et al. (2008) and Wen et al. (2004), the duration of the landslide was around 55-77 s. The average velocity varied from 13.6 m/s to 19.8 m/s, which were obtained from the numerical calculation, and estimated according to the maximum displacement of landslide and runout time, respectively (Yu and Yang, 1988 and Zhang et al., 2002).

2.3. Accumulative characteristics and consequences

Figure 8 shows the topographic feature of the study area before and after the event. Figure 9 indicates the variation of the elevation of Saleshan landslide before and after the event. Since the slope moved downward and deposited along the moving path, the negative value of the elevation variation in source area indicates a decrease in the elevation and the rest of flow channel shows an increase in the elevation. The maximum variation of the elevation is more than 130 m located at the crest of the slope. Then, the thickness of deposition ranges from very shallow to more than 30 m, which is located at the middle part deposited material. This mainly resulted from the spreading effect of moving material in the

lateral direction. The width of deposition zone varies as well, although this change in width is very limited.

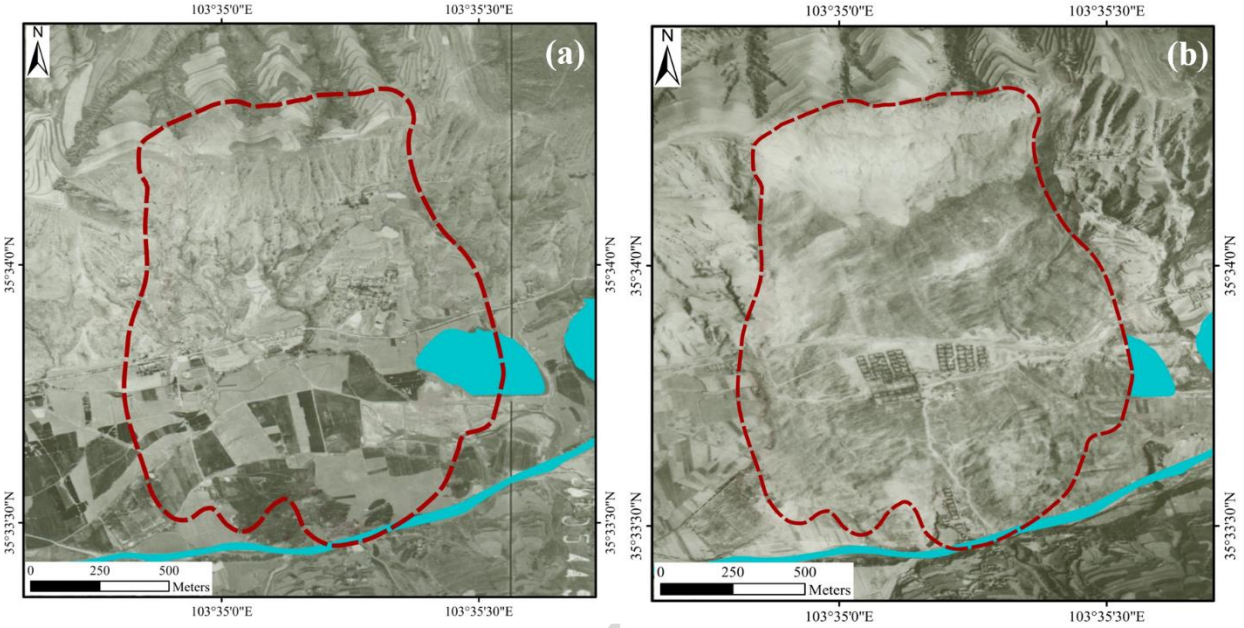

Figure 8: Aerial photos of the study area showing the change of topography, (a) Before the event (taken in June 1979); (b) After the event (taken two weeks after the landslide)

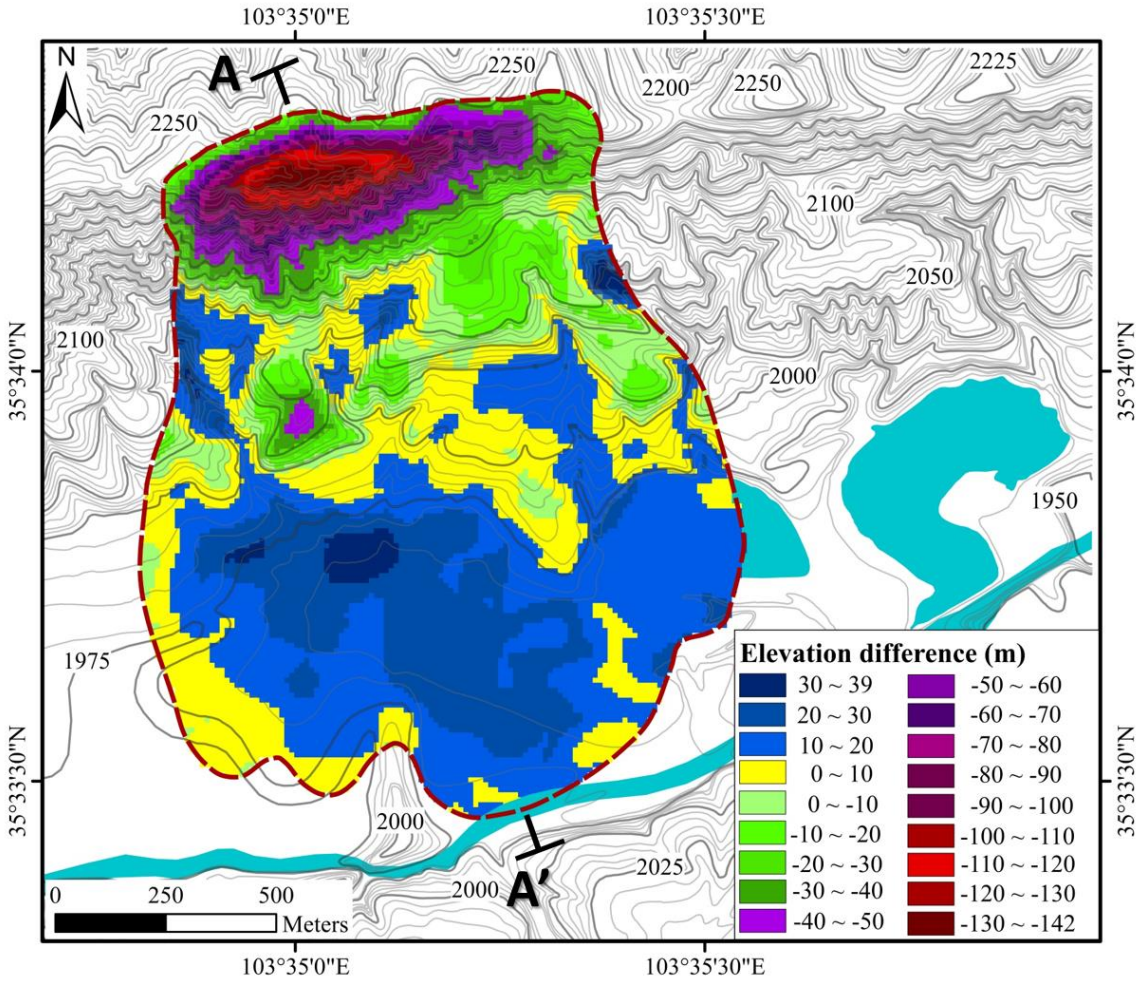

Figure 9: Elevation variation of the Saleshan landslide before and after the landslide

The total area affected by the landslide is more than 1.5 km^2 (Figure 9). Three seismic-stations near the study area all detected the vibration when the Saleshan landslide happened (Figure 10). Based on the recorded data of these seismic-stations, Zha (1983) and Cao (1986) concluded that the slope probably failed at approximately 17:48:46, accompanied by a 1.4 M_s earthquake.

Wu and Wang (2006) also reported another landslide in the same area which occurred on March 26, 1986, with a volume of 2.4×10^6 m^3 and average travel distance of approximately 250 m. The 1986 landslide left an arc pattern on the deposition material of the 1983 landslide, which is still visible on the aerial photo.

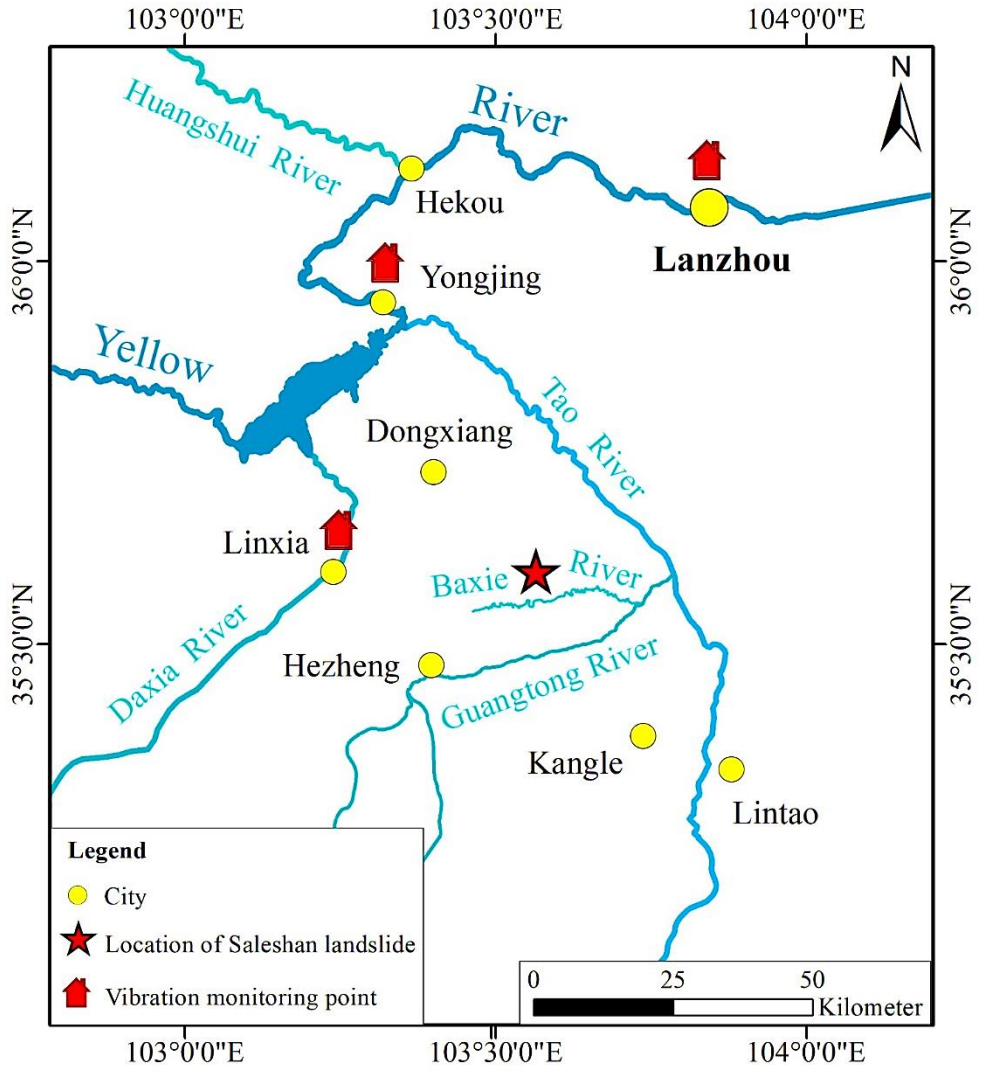

Figure 10: Location of the seismic stations and Saleshan landslide

3. Laboratory tests results

In the post-failure process, the residual strength of the soil plays an important role in the kinematic characteristics of landslides. The friction angles and cohesive strength of the loess and mudstones are obtained from direct shear tests.

Figure 11 shows the laboratory results of properties of the loess and mudstones. The maximum shear displacement of each test was 12 mm. The main loess involved in the movement was Lishi Loess (Q_2). Figure 11a indicates the shear resistance-displacement relationships under different normal stress. Peak strengths can be found from each of the lines. Figures 11b, 11c, and 11d indicate the relationships of shear resistance against shear displacement of Mudstones ($N^{L-2}{}_2$, $N^{L-3}{}_2$, and $N^{L-4}{}_2$, respectively). Strain

softening is detected in $N^{L-2}{}_2$, $N^{L-3}{}_2$, and $N^{L-4}{}_2$. One possible reason of lower strength in the Q_2 is internal weathering through the dissolution of salts as explained and demonstrated by Derbyshire et al. (1993).

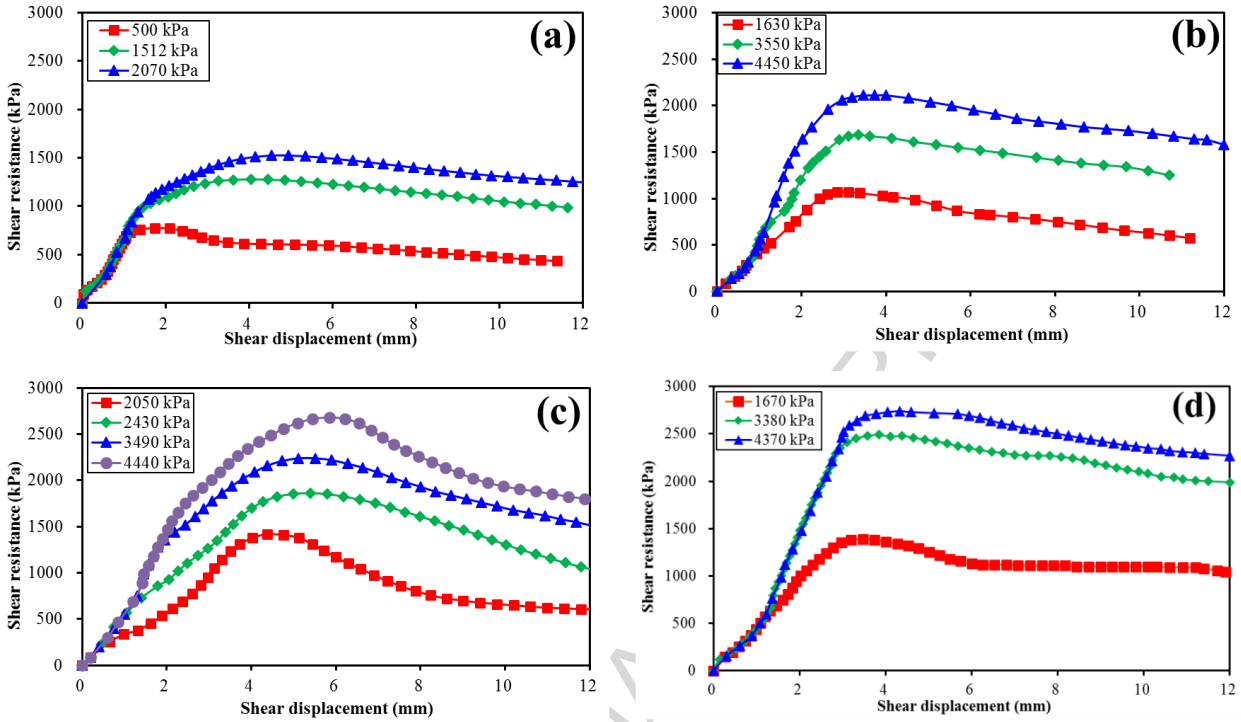

Figure 11: Shear resistance against shear displacement relationship of the soils involved in the landslide (a) Q_2 (Zhang et al., 2002) (b) $N^{L-2}{}_2$ (c) $N^{L-3}{}_2$ and (d) $N^{L-4}{}_2$

Figures 12a and 12b show the relationship between peak shear resistance and normal stress of the soils, between residual strengths and normal stress. The peak and residual frictional angles of Q_2 are both approximately 25º. However, the frictional angles corresponding to peak and residual strengths are 19.8º and 19.5º for $N^{L-2}{}_2$, 26º and 23.2º for $N^{L-3}{}_2$, and 27.2º and 25.3º for $N^{L-4}{}_2$. The peak cohesion estimated from the Figure 12a is larger than 450 kPa for Mudstones. The peak cohesion of Q_2 is higher than that obtained from tri-axial tests (Li et al., 2013), resulting from the specified shear plane in the direct shear tests. Figure 11 indicates that the residual shear strength had not been reached. Therefore, a high residual cohesion was obtained. In the following analysis, cohesion strength from Wu and Wang (2006) and internal friction angle from Li et al. (2013) are also taken into consideration.

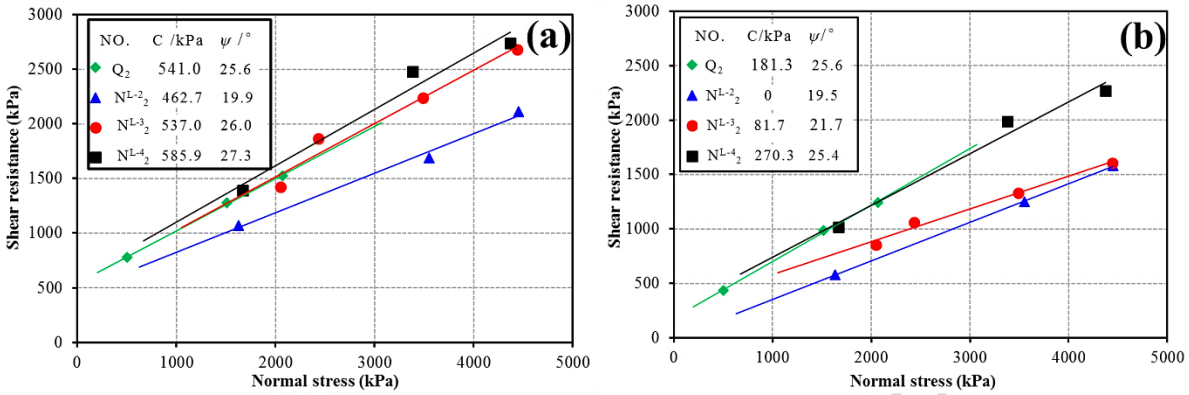

Figure 12: The laboratory results of soils. The results of N^{L-3}_2 were retrieved from Zhang et al. (2002). (a) Peak strength; (b) Residual strength

4. Numerical simulation and results analysis

Since the width of landslide path does not vary a lot, the 2D model can be used to study the kinematic characteristics of the landslides. The friction angles, cohesion strength and the density of soil in the simulation are from previous test results. The parameters were also calibrated according to the runout distance which can be observed directly through field investigation. In the initial test simulation, once runout distance showed good consistency with the field observation, so the authors fixed the parameters and then conducted the simulation again for a detailed examination of the sliding velocity. In the calibration, the frictional angles were changed according to the field situation. The original values were obtained from the published test results.

4.1. Runout model

There are several approaches that can be employed in debris flow runout modeling, including empirical approach, discontinued approach, and continuum approach (Peng et al., 2016; Calvetti et al., 2016; Thompson et al., 2009). Miao et al. (2001) had used a continuum approach to study Saleshan landslide adopting the limit equilibrium analysis approach and incorporating mass dynamics and soil deformation. In this study, an energy-based continuum model was used to study the Saleshan landslide, which also considers the internal energy dissipation due to deformation during the movement of debris flow (Wang et al., 2010; Kang and Chan, 2017).

The analytical runout model is mainly based on the Newton's Second Law or energy balance (McDougall, 2016). In the slice-based model, the energy model determines the motion of each slice based on the energy conservation equations using the Lagrangian difference scheme (Wang et al., 2008) (Figure 13). The change in kinetic energy of a sliding mass consists of changes in potential energy, work done by resistance forces along the base of the sliding mass and work due to internal deformation of the debris.

Lateral pressure and basal resistance on individual slices can be calculated using the Rankine and Mohr-Coulomb equations. The governing equation of the runout model is:

$$\frac{d}{dt}\left(\frac{1}{2}m\bar{u}^2\right) = mg\bar{u}\sin\theta + \frac{1}{2}mgh\bar{e}_{zz} + P_L\bar{u}_L\cos\theta_L - P_R\bar{u}_R\cos\theta_R - T\bar{u} - \int_V \tau_{ij}e_{ij}\,dV \qquad [1]$$

where m is the mass of the slice, $\bar{u}$ is the mean velocity of the slice along the base of the slice, g is gravity acceleration, θ is the inclination of the base of the slice with respect to the horizontal, P_L and P_R are interslice forces exerted on the left and right sides of the slice, T is the shear force acting along the base of the slice, τ_{ij} is the components of the stress tensor, and e_{ij} is the component of the strain rate tensor.

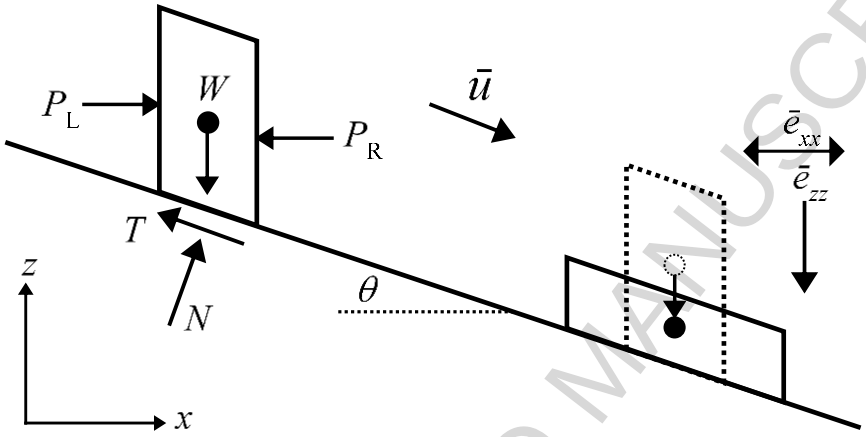

Figure 13: Schematic of forces acting on a single slice in the runout model (Zhang et al., 2017)

The runout model has been validated through studying historical cases (Wang et al., 2010). Kang et al. (2017) incorporated an entrainment model into the runout model to study an extremely large rock avalanche (Kang and Chan, 2017). The model was also used in the simulation of a flowslide occurred in Loess area of China (Zhang et al., 2017).

4.2. Constitutive model

There are different constitutive models that can be used to describe the shear behavior of soils (Guo et al., 2016; Kang and Chan, 2018). The Voellmy fluid model was initially developed for the modeling of snow avalanche motion with the assumption that shear resistance at the base of an avalanche is given by the summation of Coulomb-type friction and a turbulence term. As the Voellmy model is more appropriate for the flow slides with a significant amount of liquefied material (Hungr, 2008), it is adopted in this study, given by

$$\tau = \sigma\tan\phi + \gamma u^2/\xi \qquad [2]$$

where τ and σ are shear and normal stresses, respectively; ϕ is the basal friction angle; u is longitudinal velocity; γ is the unit weight of the material, and ξ is a turbulence coefficient with the dimension of acceleration.

4.3. Parameter setup

Soil parameters affecting the simulation are the unit weight of soil, internal and basal friction angles, cohesion, and turbulent coefficient. Zhang et al. (2002) tested the natural soil density above the sliding surface. The sliding body consisted of different layers, the density for loess varied from 15.4 kN/m^3 to 18.4 kN/m^3. For mudstone, the density was close to 21 kN/m^3. Since the main part of moving material was mudstone, 20 kN/m^3 was used as the unit weight of the soil, after the consideration of the percentage of the volume of each type of soil in the sliding body from the longitudinal profile (Xu et al., 2007). Zhang et al. (2002) and Liu et al. (2000) estimated the internal and basal friction angles, and cohesion strength according to laboratory tests. They used different basal friction angle for the soil at original position and on the sliding surface. Since kinematic characteristics of the landslide was studied, the friction angle between moving soil and sliding surface was used as basal friction angle. Internal friction angle was determined based on the laboratory results in Figure 12. Selection of turbulent coefficient referred to results of previous studies (Kang et al., 2017; Quan Luna et al., 2012). Summary of mechanical parameters is listed in Table 2.

Li et al. (2013) and Zhang et al. (2013) carried out a series of laboratory tests to obtain the effective internal friction angles of loess under different water content. Although the effective friction angle changes with the increase of moisture content of the soil, the deviation is not large. The average value of the friction angle was around 21º. Liu et al. (2000) conducted a numerical simulation of Saleshan landslide. Difference friction angles were used in the calculation. For Saleshan landslide, the moving part mainly consisted of Malan and Lishi loess which internal friction angles ranged from 28º to 34º. The internal friction angle adopted by Liu et al. (2000), 22º, was initially used in this study and then calibrated based on runout distance.

Liu et al. (2000) used 3º-5º as the basal friction angle in the simulation. Su (1986) considered that the basal friction angle was 6º-14º. Since the alluvial sand layer could be liquefied in the movement, a smaller friction angle due to the liquefaction could be used. Therefore, a basal friction angle of 6º was used reasonably in the simulation after calibration.

The turbulent coefficient is a function of hydraulic radius and Manning's roughness coefficient. Hydraulics radius depends on the geometrical property of the flow channel. The roughness coefficient is related to the roughness of the flow channel which means the roughness of the flow channel determines

the value of the turbulent coefficient. The value used in this study was close to that suggested by Quan Luna et al. (2012) and Xu et al. (2012).

Calibration of the parameters in the numerical simulation sometimes is necessary since it is very difficult to use only one or two parameters to represent the dynamic characteristics of the soil. However, the calibration should be based on test results and cannot deviate far away from the tested results. In the simulation, the runout distance was adopted as a criterion in the calibration.

Table 2 Mechanical properties of soil used in the simulation

Parameters	Values
Unit weight (kN/m^3)	20
Internal friction angle (°)	25
Basal friction angle (°)	6
Cohesion (kPa)	1
Turbulent coefficient (m/s^2)	300

4.4. Simulation results

Using the parameters in Table 2, the simulation lasts 69 s. The energy dissipation during the simulation is composed of two parts: one is due to basal friction, and another is due to the deformation of the moving soil. The soil movement mainly occurs in approximately 60 s. Therefore, the variation of moving soil profiles with 10 s interval is shown in Figure 14.

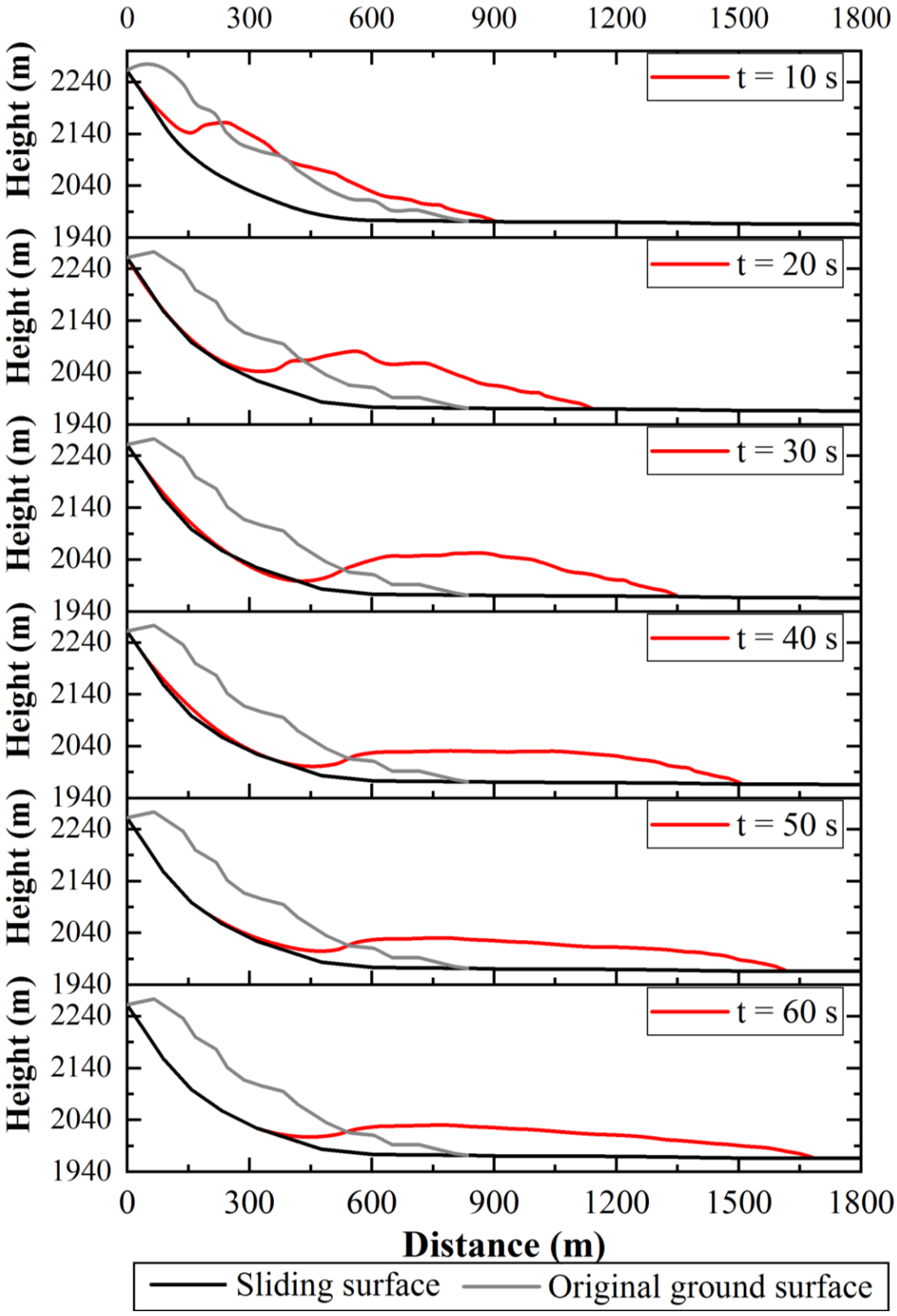

Figure 14: Variation of Saleshan profile against calculation time

In the simulation, all the slices stop the movement after 69 s which is very close to the description by Li et al., (2008) showing the landslide lasted 77 s. Wu and Liu (1983) also showed that the landslide finished the movement in approximately 1 minute. Liu et al. (2000) and Miao et al. (2001) calculated the kinematic characteristics of the landslides showing the landslide stopped moving in 87 s. Overall, the calculation time is very close to the field observation and previous calculation results. However, since the actual moving time was not recorded, the total moving time can only be compared with that from previous results by Zhang et al. (2002) and Miao et al. (2001).

In the movement as shown in Figure 14, the excess pore water pressure existed underneath the landslide body (Figure 6e), resulting in a very lower residual strength along the moving path. After the landslide stopped, dissipation of the pore water pressure commenced.

4.4.1. Velocity

Figure 15 indicates the velocities of all the slices along the channel bed in each 10 s. The frontal velocities are also included in the figure. The frontal velocity reaches the maximum values, 25.2 m/s when the soil moves to approximately 1100 m. After that, the soil starts to decrease until it finally stops. After around 10 s, the maximum velocity is detected at the front of the moving soil showing the front of soil moves faster.

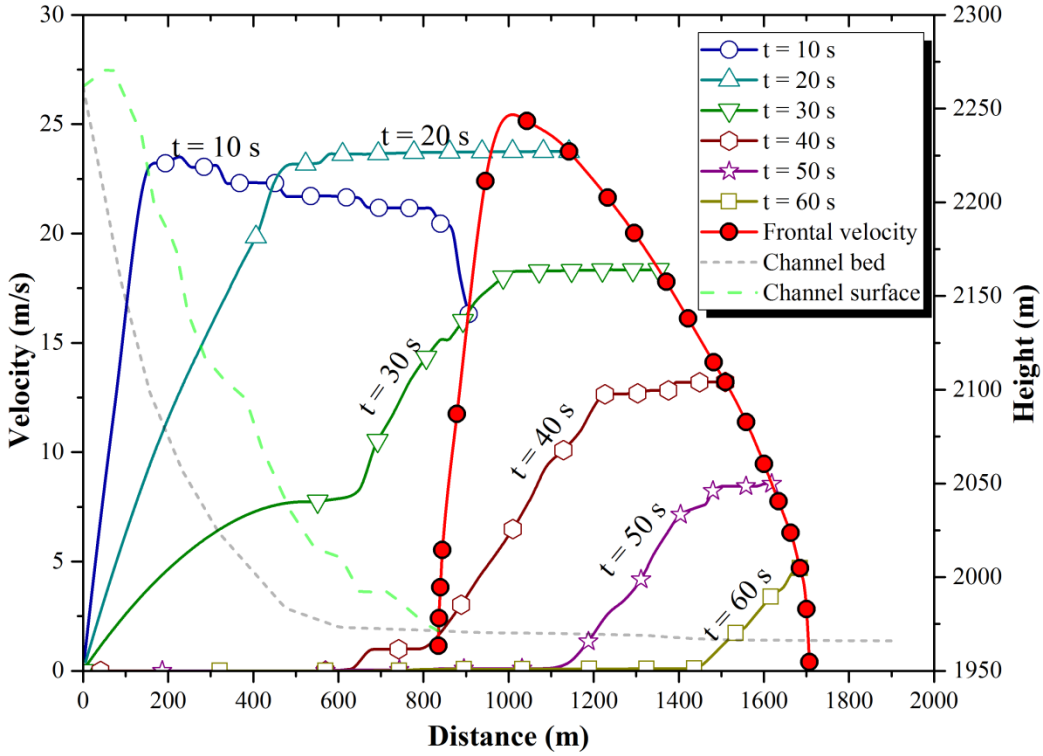

Figure 15: Calculated velocities of moving soil with a 10 s interval

Since maximum velocity is very difficult to obtain when the landslide occurred, an indirect method is used to estimate the velocity. According to the travel distance and estimated traveling time of the survivor working on the slope, the estimated maximum velocity is approximately 30 m/s. Miao et al. (2001) calculated the maximum velocity at the front of moving soil, equal to 32.5 m/s. Figure 16 indicates the comparison results of the velocities. The maximum calculated velocity is very close to previous simulation results. Yu and Yang (1988) also estimated the average velocity. A range between 13.6 and 17.2 m/s was provided. The average velocity from the calculation is 12.7 m/s that also agrees with the results from Yu and Yang (1988).

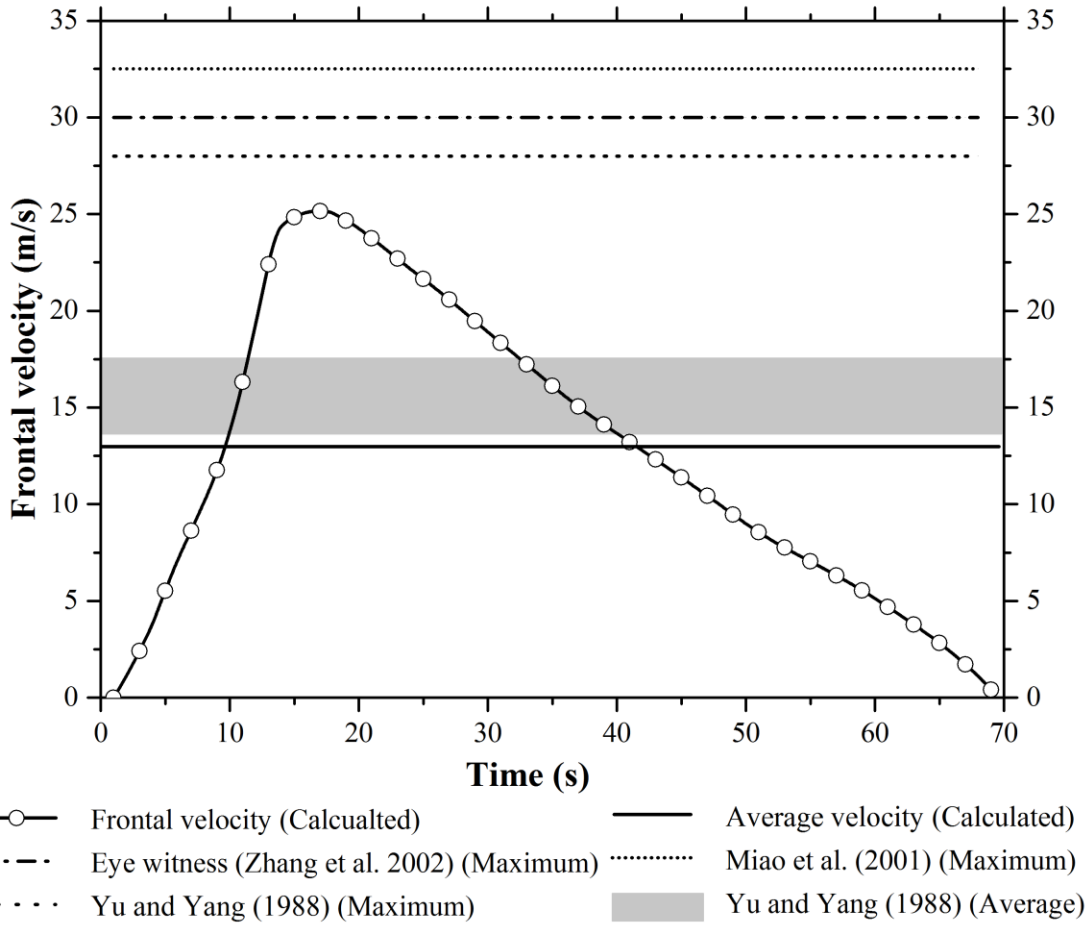

Figure 16: Comparison of calculated velocities with observation and previous results

4.4.2. Variation of runout distance and maximum height

According to Figure 17, runout distance increases slowly at initial 6 s. After that, it increases rapidly until t = 17 s. Then, the increase rate of runout distance starts to decrease. The maximum height of soil starts with 116 m. After 39 s, the height decreases to 62 m and keeps constant until the end of the

movement. Kang et al. (2017) studied the Yigong rock avalanche and observed that the maximum height would be smaller if the lateral spreading effect is taken into account.

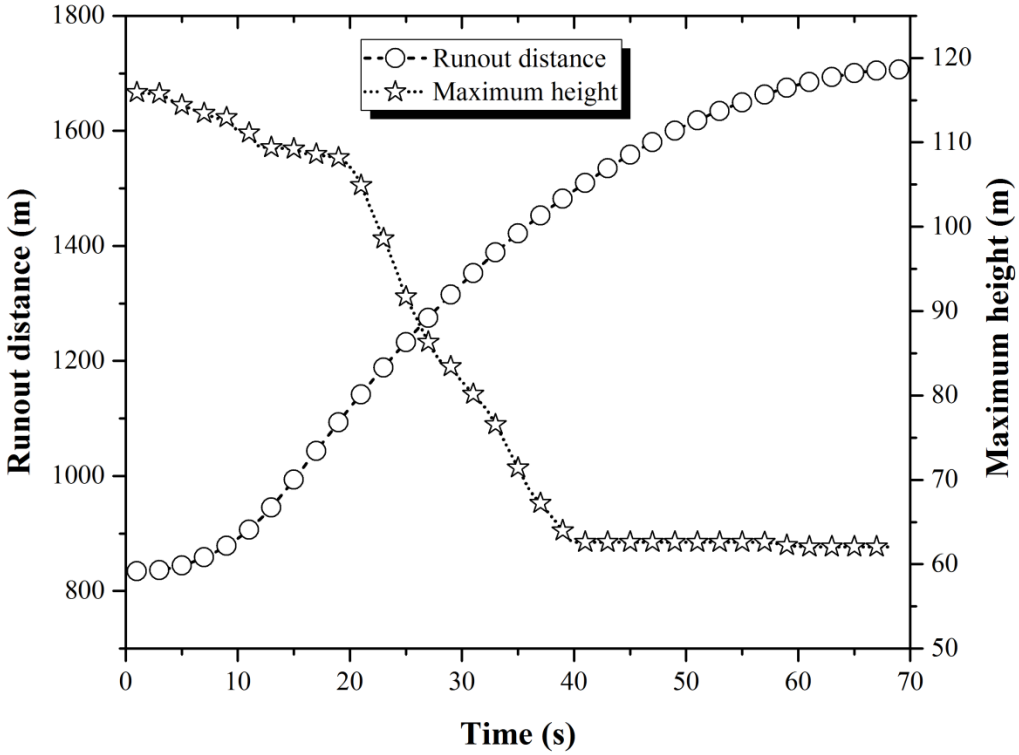

Figure 17: Variation of runout distance and maximum flow height against time

According to the profile of the landside before and after the event, the landslides moved around 1700 m until it finally met the Baxie river and climbed up the south bank of the river. Miao et al. (2001) observed that the toe the landslide traveled with a distance of less than 1300 m.

The maximum deposition height after the event is more than 60 m which is larger than that estimated according to the DEMs (Figure 9). The difference may result from the accuracy of the DEMs and also the negligence of lateral spreading effect.

4.4.3. Parametric study

The effect of two most significant parameters was also studied including basal friction and internal friction angles. The effect of them is shown in terms of runout distance and maximum front velocity. Figure 18a demonstrates the effect of internal friction angle on runout distance and maximum front velocity. When internal friction angle increases from 15º to 35º, maximum frontal velocity decreases from 25.5 m/s to 23.5 m/s. However, runout distance decreases from 1868 m to 1532 m. Figure 18b gives out similar information when basal friction angle increases from 4º to 8º.

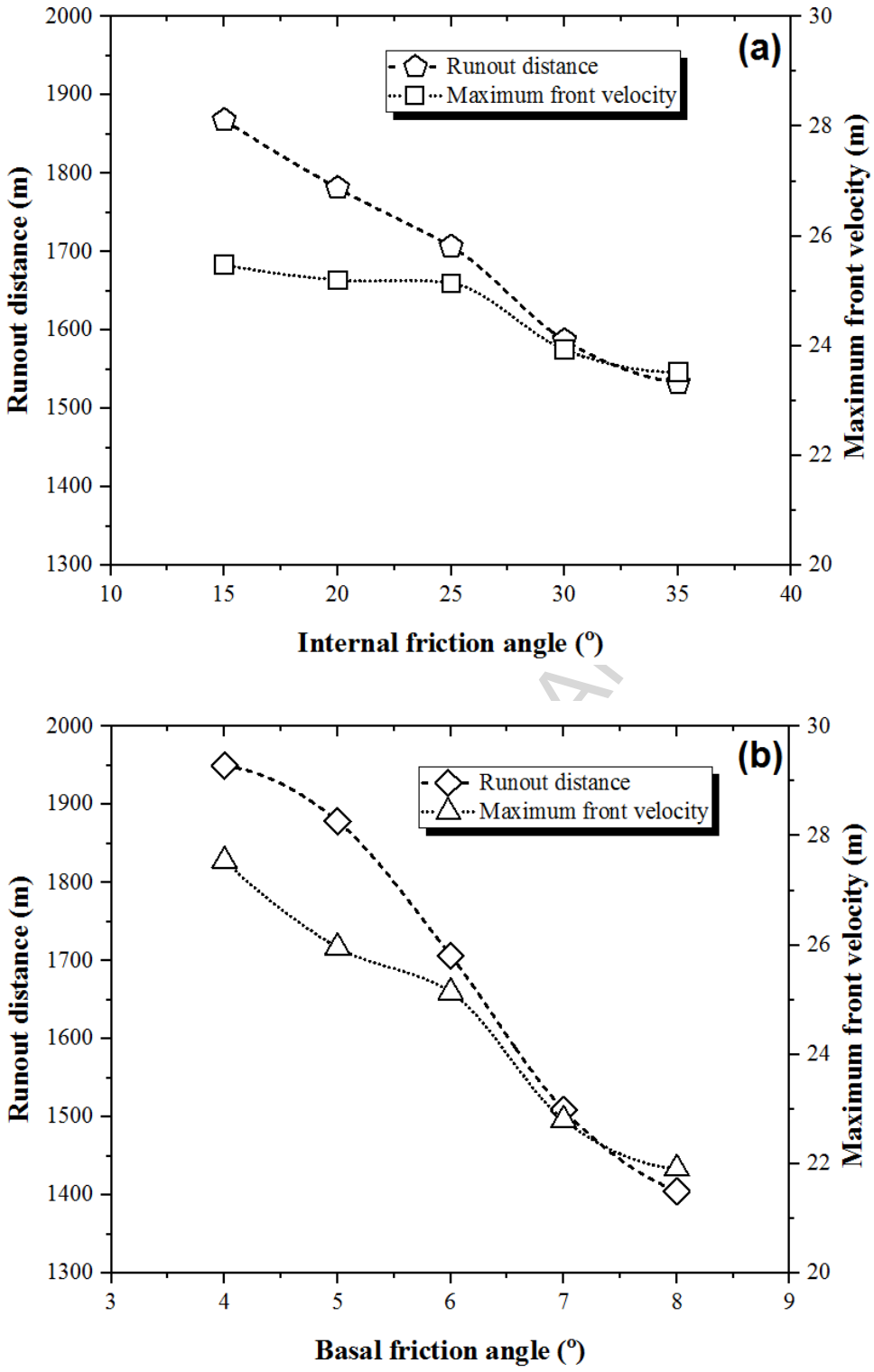

Figure 18: Sensitivity analysis results of internal and basal friction angles. (a) Effect of internal friction angle on runout distance and maximum front velocity; (b) Effect of basal friction angle on runout distance and maximum front velocity

5. Discussion and conclusions

Figure 19a indicates the precipitation before and after the event. The accumulative precipitation before the event in 1983 was around 15 mm, and no precipitation was recorded three days before the Saleshan landslide. In 1982, the accumulated rainfall was approximately 430 mm, close to the average annual precipitation that is 485 mm. However, the precipitation from October to December in 1982 was 66.3 mm, seven times more than the average precipitation in the same period previous years (Han, 1986). This would very likely result in a larger variation of the underground water table in the following few months, compared with the resulted variation of the water table in the previous years.

Figure 19b shows average temperature in 1983. In January and February, the average temperatures were -8.2 ℃ and –4.4 ℃. However, the average temperature rose up to 0.9 ℃, which probably caused an increase of water table as the result of the infiltration of meltwater along the seepage path located in the slope (Xiao et al., 2017).

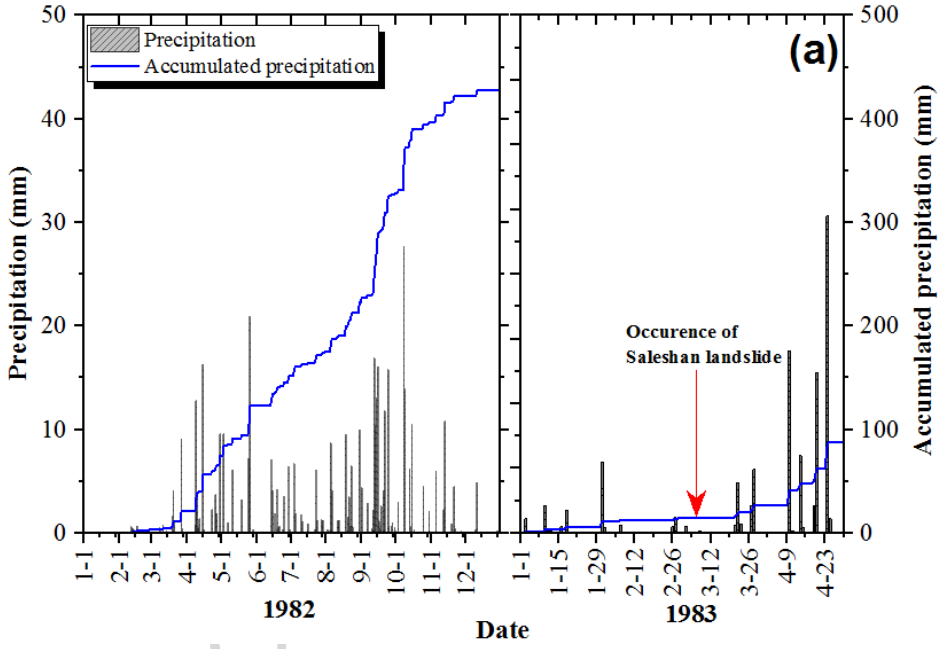

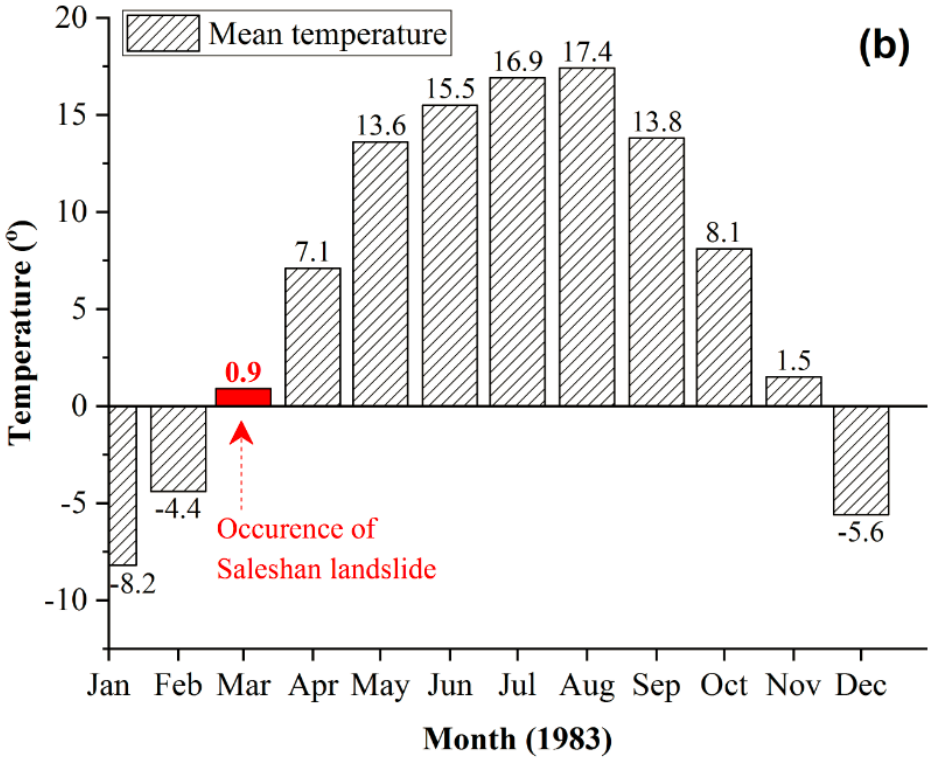

Figure 19: Meteorological data of the study area (a) Precipitation before and after the event at Linxia meteorological station. (b)The mean temperature at Linxia meteorological station in 1983

The cracks behind the crest of the slope and fissures developed in the soil accelerated the infiltration of the water (Figure 5). The cracks can also store the perched water to supplement the groundwater. The infiltration of water played a significant role in the progressive failure process which could lead to the reduction of shear resistance that can further accelerate the failure process. In the post-failure process, the existing water in the sliding zone significantly decreased the shear resistance of the soil in the sliding zone and decreased the effective stress applied on the alluvial sand due to the excess pore water pressure.

The sliding zone in the slope was developed progressively, and the landslide exited from the bottom of the slope. The weathering and loss of structural strength resulted in the development of fissures and cracked in the soil. A local shear surface was then formed after a long period and extended to the toe of the slope and bottom of the tension cracks behind the slope, as proposed by Petley et al. (2005). The comparison of the DEMs before and after the event together with the borehole information indicated that the toe of the slope had been mobilized and landslide exited from the toe of the slope.

The liquefaction of the alluvial sand could be the main reason for a long travel distance of the landslide. The low water table in the terrace I and water supply from precipitation, meltwater, and irrigation together provided the possibility of the liquefaction. The soil samples investigated by Wu and

Wang (2006) also verify the existence of soil liquefaction. This evidence supports the hypotheses that the long travel distance resulted from the liquefaction of soil layer. Peng et al. (2018) observed the similar failure mechanism and kinematic characteristics from the landslides in South Jingyang Platform.

Calibration and parameter selection in the simulation are very critical problems (McDougall, 2016; Cui et al., 2017; Tang et al., 2017). There are two approaches to select the input parameter values. One is to use the values measured in the field or laboratory (Iverson and George, 2016). Another approach is to base inputted parameters on the calibration (Kang et al., 2017; Hungr, 1995). In this paper, the parameter selection was based on the laboratory test with calibration. In the model calibration, the final runout distance was measured according to the final deposition location. However, since the landslide stopped as it moves up against the river terrace at the far side of the valley, using this distance in the calibration would lead to the underestimation of the mobility of the landslide, which can be observed from Figure 16, although the longitudinal profile in the simulation was exported from actual DEM.

According to parametric study, the runout distance of the landslide is mostly affected by basal and internal friction angles. Increasing the basal friction angle from 4º to 8º can result in a 27.8% decrease of runout distance and 20.3% of maximum frontal velocity. However, the increase of internal frictional angle from 15º to 35º leads to 17.9% reduction of runout distance and 7.5% reduction of maximum frontal velocity. The differences demonstrate that the effect of friction angles is significant on the runout distance. Overall, the results from the energy-based runout model agree with previous simulation results. This model provides an alternative solution to study landslides in the loess area.

Acknowledgment:

This paper is supported by Major Program of National Natural Science Foundation of China (No. 41790443), the National Natural Science Foundation of China (No. 41401040 and No. 41362014), Project of Geological Disaster Emergency Capacity of Department of Land and Resource in Gansu Province, China (No. GSZYTC-ZC-18005), and Opening fund of Key Laboratory of Mechanics on Disaster and Environment in Western China (No. 201701). We would also very like to thank three anonymous reviewers for their help in improving the content of the paper.

References

Calvetti, F., Prisco, C. G., and Vairaktaris, E. (2016). DEM assessment of impact forces of dry granular masses on rigid barriers. *Acta Geotechnica*, 12(1), 129-144.

Cao, B., 1986. The geologic characteristics of the Sale Shan type of super landslide and a model for spatial prediction. In Proc. of Fifth International Association of Engineering Geology International Congress. 3, pp. 1989-1997.

Chen, G., Feng, X.D., and Gao, L. (2012). The comparison of the characteristics of the landslides in Lanzhou, Gansu. *Science and Technology Vision*. 14, 134-135, and 214. (in Chinese)

Cui, Y. F., Chan, D., Nouri, A. (2017). Coupling of Solid Deformation and Pore Pressure for Undrained Deformation – a Discrete Element Method Approach. *International Journal for Numerical and Analytical Methods in Geomechanics*. 41(18), 1943-1961.

Derbyshire, E., Dijkstra, T.A., Billard, A., Muxart,T., Smalley, I.J. and Li, Y.J. (1993). Thresholds in a sensitive landscape: the loess region of central China. In: Thomas, D.S.G. and Allison, R.J. (eds.) Landscape Sensitivity, John Wiley and Sons Limited, Chichester and New York, 97-127.

Derbyshire, E., Meng, X. and Dijkstra, T.A. (2000). Landslides in the thick loess terrain of north-west China. John Wiley & Sons Incorporated, pp 1–256.

Guo, X., Peng, C., Wu, W., and Wang, Y. (2016). A hypoplastic constitutive model for debris materials. *Acta Geotechnica*, 11(6), 1217-1229.

Han, K. Z. (1986). The correlation between human activities and Saleshan landslide. Journal of Catatrophology, 1(4): 64-66. (in Chinese)

Huang, R. Q. (2007). Large-scale landslide and their sliding mechanisms in China since the 20th Century. *China Journal of Rock Mechanism and Engineering*, *26*(3), 433-454. (in Chinese)

Huang, R. Q. (2009). Some catastrophic landslides since the twentieth century in the southwest of China. *Landslides*, 6(1), 69-81.

Huang, R. Q., Chen, G. Q., Guo, F., Zhang, G. F., and Zhang, Y. (2016). Experimental study on the brittle failure of the locking section in a large-scale rock slide. *Landslides*, 13(3), 583-588.

Huang R.Q. (2007). Large-scale landslides and their sliding mechanisms in China since the 20th century. *Chinese Journal of Rock Mechanics and Engineering*, 3(3), 433-454

Hungr, O. (1995). A model for the runout analysis of rapid flow slides, debris flows, and avalanches. *Canadian Geotechnical Journal*, 32(4), 610-623.

Hungr, O. (2008). Numerical modeling of the dynamics of debris flows and rock avalanches. *Geomechanics and Tunnelling*, 1(2), 112-119.

Hungr, O., Leroueil, S. and Picarelli, L. (2014). The Varnes classification of landslide types, an update. Landslides, 11(2), 167-194.

Iverson, R. M. (1997). The physics of debris flows. Reviews of Geophysics, 35(3), 245-296.

Kang, C., and Chan, D. (2017). Modelling of Entrainment in debris flow analysis for dry Granular Material. *International Journal of Geomechanics (ASCE)*, 17(10), DOI:10.1061/(ASCE)GM.1943-5622.0000981.

Kang, C. and Chan, D. (2018). Numerical simulation of 2D granular flow entrainment using DEM. Granular Matter, 20(1), 13. https://doi.org/10.1007/s10035-017-0782-x

Kang, C., Chan, D., Su, F. H., and Cui, P. (2017). Runout and entrainment analysis of an extremely large rock avalanche—a case study of Yigong, Tibet, China. *Landslides*, 14(1), 123-139.

Li, B., Wu, S.R. and Shi, J.S., (2011). Research on development characteristics and distribution of landslides in Weibei Loess tableland area. *Research of Soil and Water Conservation*, 18(5), 212-216. (In Chinese)

Li, T. L., Wang, P., and Xi, Y. (2013). The mechanisms for initiation and motion of Chinese loess landslides Progress of Geo-Disaster Mitigation Technology in Asia. pp. 105-122, Springer Berlin Heidelberg.

Li, X. Z., Kong, J. M., and Wang, C. H. (2008). Gauss-Newton method and its application in parameter optimization of landslide prediction model. *Bulletin of Soil and Water Conservation*, *28*(5), 132-135. (in Chinese)

Li, X. Z., Kong, J. M., and Wang, Z. Y. (2012). Landslide displacement prediction based on combining method with optimal weight. *Natural Hazards*, *61*(2), 635-646.

Liu, Z. Y., Ma, C. W., Miao, T. D., and Mu, Q. S. (2000). Kinematic block model of long run-out prediction for high-speed landslides. *Chinese Journal of Rock Mechanics and Engineering*, 19(6), 742-746. (in Chinese)

Luna, B. Q., Remaitre, A., van Asch, T. W. J., Malet, J. P., and van Westen, C. J. (2012). Analysis of debris flow behavior with a one dimensional run-out model incorporating entrainment. *Engineering Geology*, *128*, 63-75.

Lv, H. T., Yang, S. Q., and Ai, N. S. (1984). On the connection between the landslide at Sale Mountain and the neotectonic stress field. *Journal of Lanzhou University (Natural Sciences)*, 20(4), 96-104. (in Chinese)

McDougall, S. (2016). 2014 Canadian Geotechnical Colloquium: Landslide runout analysis — current practice and challenges. *Canadian Geotechnical Journal*, *54*(5), 605-620.

Miao, T. D., Liu, Z. Y., Niu, Y. H., and Ma, C. W. (2001). A sliding block model for the runout prediction of high-speed landslides. *Canadian Geotechnical Journal*, *38*(2), 217-226.

Peng, C., Guo, X., Wu, W., and Wang, Y. (2016). Unified modelling of granular media with Smoothed Particle Hydrodynamics. *Acta Geotechnica*, 11(6), 1231-1247.

Peng, J., Ma, P., Wang, Q., Zhu, X., Zhang, F., Tong, X., Huang, W. (2018). Interaction between landsliding materials and the underlying erodible bed in a loess flowslide. *Engineering Geology*, 234, 38-49.

Petley, D.N., Higuchi, T., Petley, D.J., Bulmer, M.H. and Carey, J. (2005). Development of progressive landslide failure in cohesive materials. *Geology*, 33(3), 201-204.

Petley, D. (2012). Global patterns of loss of life from landslides. *Geology*, 40(10), 927-930.

Su, B. L. (1986). Research on the mechanism of the Sale Mountain Landslide. *Journal of Hebei College of Geology*, *9(3-4), 327-346.* (in Chinese)

Tang, Y., Chan, D. H., and Zhu, D. Z. (2017). A coupled discrete element model for the simulation of soil and water flow through an orifice. *International Journal for Numerical and Analytical Methods in Geomechanics*, 41(14), 1477-1493.

Thompson, N., Bennett, M.R., and Petford, N. (2009). Analyses on granular mass movement mechanics and deformation with distinct element numerical modeling: implications for large-scale rock and debris avalanches. *Acta Geotechnica*, 4(4), 233-247.

Wang, G. H., Zhang, D. X., Furuya, G., and Yang, J. (2014). Pore-pressure generation and fluidization in a loess landslide triggered by the 1920 Haiyuan earthquake, China: A case study. *Engineering Geology*, 174, 36-45.

Wang G.X. (1988) Review on landslide research and prevention (in Chinese). In: Proc Symp Landslides, Lanzhou. China Railway Press, pp 5–18.

Wang, S.T., Zhang, Z.Y., Zhan, Z., and Liu, H.C. (1988). On the characteristics and dynamics of the catastrophic Mount Sale landslide, Gansu, China. *Journal of Chengdu College of Geology*, 15(2), 58-63. (in Chinese)

Wang, X.B., Morgenstern, N.R., Chan, D.H.. (2010). A model for geotechnical analysis of flow slides and debris flows. *Canadian Geotechnical Journal*, 47, 1401-1414.

Wen, B. P., Wang, S. J., Wang, E. Z., and Zhang, J. M. (2004). Characteristics of rapid giant landslides in China. *Landslides*, 1(4), 247-261.

Wu, Q. W., and Liu, X. M. (1983). The prediction of large landslide in loess area: a case study of Saleshan landslide. *Bulletin of Soil and Water Conservation*, 3, 82-87. (in Chinese)

Wu, W.J., and Wang, N.Q. (2006). Landslide hazards in Gansu. Gansu, China: Lanzhou University Press.

Wu, W.J., and Wang, S.Y. (1989) The mechanism of Saleshan Landslide. National landslide conference—landslides. Sichuan Science and Technology Press, Chengdu, pp 184–189.

Xiao, Z.A., Lai, Y.M., and Zhang, M.Y. (2017). Study on the freezing temperature of saline soil. *Acta Geotechnica*, 1-11.

Xu, Q., Shang Y.J., Van Asch, T.W.J., Wang, S.T., Zhang, Z.Y., and Dong, X.J. (2012). Observations from the large, rapid Yigong rock slide– debris avalanche, southeast Tibet. *Canadian Geotechnical Journal*, 49(5), 589- 606.

Xu, C., Xu, X. W., Shyu, J. B. H., Zheng, W., and Min, W. (2014). Landslides triggered by the 22 July 2013 Minxian–Zhangxian, China, Mw 5.9 earthquake: Inventory compiling and spatial distribution analysis. *Journal of Asian Earth Sciences*, 92, 125-142.

Xu, Z. J. Lin, Z. G., and Zhang, M. S. (2007). Loess in china and loess landslides. *Chinese Journal of Rock Mechanics and Engineering*, 26(7), 1297-1312. (in Chinese)

Yu, R. F., and Yang, Y. Q. (1988). Study of the characterisitics of Saleshan landslide. *Water Resources and Hydropower Engineering*, 6, 13-17. (in Chinese)

Zha, X. G. (1983). Fault together with water and gravity force resulting in the failure of Saleshan landslide. *Bulletin of Soil and Water Conservation*, 3, 27-33. (in Chinese)

Zhang, D. X., Wang, G. H., Luo, C. Y., Chen, J., and Zhou, Y. X. (2009). A rapid loess flowslide triggered by irrigation in China. *Landslides*, *6*(1), 55-60.

Zhang J.W. (1983). The investigation report of Saleshan Landslide. Bulletin of Soil and Water Conservation. 3, 2-7.

Zhang, F.Y, Wang, G.H., Kamai, T., Chen, W.W., Zhang, D.X., and Yang, J. (2013). Undrained shear behavior of saturated loess at different concentrations of sodium chlorate solution. Engineering Geology 155, 69-79.

Zhang, F. Y., Wang, G. H., Kamai, T., and Chen, W. W. (2014). Effect of pore-water chemistry on undrained shear behaviour of saturated loess. *Quarterly Journal of Engineering Geology and Hydrogeology*, *47*(3), 201-209

Zhang, F. Y., Kang, C., Chan, D., Zhang, X.C., Pei, X.J., and Peng, J. B. (2017). A study of a flow slide with significant entrainment in loess areas in China. *Earth Surface Processes and Landforms*, 42(14), 2295-2305.

Zhang, F.Y., and Wang, G. H. (2018). Effect of irrigation-induced densification on the post-failure behavior of loess flowslides occurring on the Heifangtai area, Gansu, China. *Engineering Geology*. 236, 111-118

Zhang, F. Y., Chen, W. W., Liu, Gao, Liang, S. Y., Kang, C., He, F. G. (2012). Relationships between landslide types and topographic attibutes in a loess catchment, China. Jouranl of Mountain Sceience, 9(6), 742-751

Zhang, F., and Huang, X. (2018). Trend and spatiotemporal distribution of fatal landslides triggered by non-seismic effects in China. Landslides, doi:10.1007/s10346-10018-11007-z.

Zhang, Z.Y., Chen, S. M., and Tao, L. J. (2002). 1983 Sale Mountain landslide, Gansu Province, China. *Reviews in Engineering Geology, 15*, 149-164.

Zhang Z.Y., and Wang S.T. (1984). On the prediction of the occurrence time and the velocity of a potential landslide, *in Proceedings, 4th International Symposium on Landslides*, Volume 3: Toronto, Canada, p. 145-146.

Zhou, J., Zhu, C., Zheng, J., Wang, X., and Liu, Z. (2002). Landslide disaster in the loess area of China. *Journal of Forestry Research*, 13, 157-161.

Zhuang, J. Q., Peng, J. B., Wang, G. H., Javed, I., Wang, Y., and Li, W. (2017). Distribution and characteristics of landslide in Loess Plateau: A case study in Shaanxi province. *Engineering Geology*. doi:https://doi.org/10.1016/j.enggeo.2017.03.001.

Highlights

- Review of previous studies of 1983 Saleshan landslide with rapid velocity and long run-out distance
- Analysis and discussion of the possible failure mechanism and post-failure process of the Saleshan landslide
- Analysis of the variation of geomorphological characteristics of the landslide
- Numerical simulation of the kinematic characteristics of the landslide